# Dynamic inflow and unsteady aerodynamics models for modal and stability analyses in OpenFAST

**E Branlard[1], B Jonkman[2], G R Pirrung[3], K Dixon[2] and J Jonkman[1]**

[1] National Renewable Energy Laboratory, Golden CO, 80401, USA
[2] Envision Energy USA Ltd., Boulder, CO, 80302, USA
[3] Technical University of Denmark (DTU) Wind Energy, Roskilde, DK-4000, Denmark

E-mail: emmanuel.branlard@nrel.gov

**Abstract.** This work presents two aerodynamic models that are used to perform modal and stability analyses of wind turbines. Including aerodynamic effects in stability analyses is important to capture aerodynamic inertia, stiffness, and damping. The two models consist of a dynamic inflow model based on Øye's model and an unsteady aerodynamics model based on a simplified Beddoes-Leishman dynamic stall model. Both models are written in a continuous-time state-space form, which is the form needed to perform linearizations within OpenFAST. In this article, we present the new models, perform some simple verifications against HAWC2 results, and then perform stability analyses. We investigate the contribution of the aerodynamic effects on the turbine modes, particularly the flapwise modes, which are the most affected. Because of the development presented in this work, Campbell diagrams accounting for dynamic stall and dynamic wake effects were generated for the first time using OpenFAST.

## 1. Introduction

The rotors of modern wind turbines are lighter and more slender than previous generations of wind turbines, resulting in more compliant structures. Maintaining aeroelastic stability is important to avoid unexpected failures of these large structures. Blade edgewise instabilities have often been a topic of concern, which was recently backed by experimental results [1]. Aeroelastic stability is usually studied using a linearization of the turbine model [2, 3] combined with a multiblade coordinate transformation [4]. The open-source multiphysics tool OpenFAST, developed by the National Renewable Energy Laboratory (NREL), has the ability to perform time simulations of land-based and offshore horizontal-axis wind turbines and generate linearized representations of the underlying nonlinear system [3, 5]. OpenFAST linearizations are obtained using a combination of analytical expressions and finite differences obtained from the same code base as the time-simulation code. In the current implementation of OpenFAST, linearization is only available for a subset of modules and options. One design choice that limits the linearization is the fact that the modules to be linearized should not include discrete-time states. This limitation affects two important aerodynamic submodules of OpenFAST: the dynamic inflow and the unsteady airfoil aerodynamics (e.g., dynamic stall) submodules. This work presents the changes we introduced to be able to include these aerodynamic effects within the linearization functionality. Both effects have important aerodynamic damping contributions and potential stiffening and inertial contributions that were not accounted for in previous releases of the linearization functionality of OpenFAST.

In this work, we describe the implementation of the two aerodynamic models added to OpenFAST: a dynamic inflow model, inspired by the work of Øye [6], and a variation of the unsteady aerodynamics model of Hansen, Gaunaa, and Madsen (known as the HGM model) [7], which is based on the work of Beddoes and Leishman [8]. The dynamic stall model of Øye [9] was also implemented as part of this work because it is a natural simplification of the HGM model. The newly implemented models use a continuous-time state-space formulation, which allows for the linearization of the models within OpenFAST. The models can also be used for time-domain analyses, leading to consistent results between the two approaches.

We start by presenting the two models as implemented in OpenFAST. Then, we present applications and verifications of the individual models. Last, we perform linearization analyses of the NREL 5-MW wind turbine to show the contribution of the new models to system frequencies and damping. Comparisons with HAWC2 [10, 11] and HAWCStab2 [12] are included.

## 2. Continuous dynamic inflow and unsteady aerodynamics models

In this section, we present the two new aerodynamic models that we implemented in OpenFAST. Both models use a continuous-time state-space formulation, and an analytical linearization of the model can be readily obtained. In the current implementation, we use a finite difference approach instead of analytical gradients; these expressions are not presented here.

### *2.1. Dynamic inflow model*

The baseline dynamic inflow model of OpenFAST corresponds to a discrete-time implementation of the model of Øye [6, 13]. The discrete form of Øye's model is the most common form found in aeroelastic codes. For details on the discrete implementation, the reader is referred to [13]. In this work, we present a continuous-time state-space formulation of the model.

Øye's dynamic inflow model relies on two time constants, $\tau_1$ and $\tau_2$:

$$\tau_1 = \frac{1.1}{1 - 1.3\min(\overline{a}, 0.5)}\frac{R}{\overline{U}_0}, \qquad \tau_2 = \left[0.39 - 0.26\left(\frac{r}{R}\right)^2\right]\tau_1 \tag{1}$$

where $R$ is the rotor radius, $\overline{U}_0$ is the average wind speed over the rotor, $\overline{a}$ is the average axial induction over the rotor, and $r$ is the radial position along the blade. The rule of thumb $\tau_1 \approx 0.2R$ can be used to estimate the value of the time constant, with 0.2 having units in s/m. The model consists of two first-order differential equations:

$$\begin{aligned} \boldsymbol{W}_{\text{int}} + \tau_1 \dot{\boldsymbol{W}}_{\text{int}} &= \boldsymbol{W}_{\text{qs}} + k\tau_1 \dot{\boldsymbol{W}}_{\text{qs}} \\ \boldsymbol{W} + \tau_2 \dot{\boldsymbol{W}} &= \boldsymbol{W}_{\text{int}} \end{aligned} \tag{2}$$

where $\boldsymbol{W}$ is the actual induction at the rotor (at a given blade position and radial position), $\boldsymbol{W}_{\text{qs}}$ is the quasi-steady induction, $\boldsymbol{W}_{\text{int}}$ is an intermediate value coupling the quasi-steady and the actual inductions, and $\dot{(\cdot)}$ represents the time derivative. The coupling constant $k$, with values between 0 and 1, is usually chosen as $k = 0.6$. The steady solution of the systems leads to $\boldsymbol{W} = \boldsymbol{W}_{\text{qs}}$. The quasi-steady (qs) induction factors $a_{\text{qs}}$ and $a'_{\text{qs}}$ are computed by a quasi-steady blade element momentum (BEM) algorithm. The quasi-steady induction vector is then determined as:

$$\boldsymbol{W}_{\text{qs}} = -a_{\text{qs}} V_x \boldsymbol{e}_x + a'_{\text{qs}} V_y \boldsymbol{e}_y \tag{3}$$

where $\boldsymbol{V}$ is the vector representing the relative motion of the airfoil (wind and elastic) without the induced velocity. The relative wind is then $\boldsymbol{U} = \boldsymbol{V} + \boldsymbol{W}$. The notations are illustrated on the left side of Figure 1.

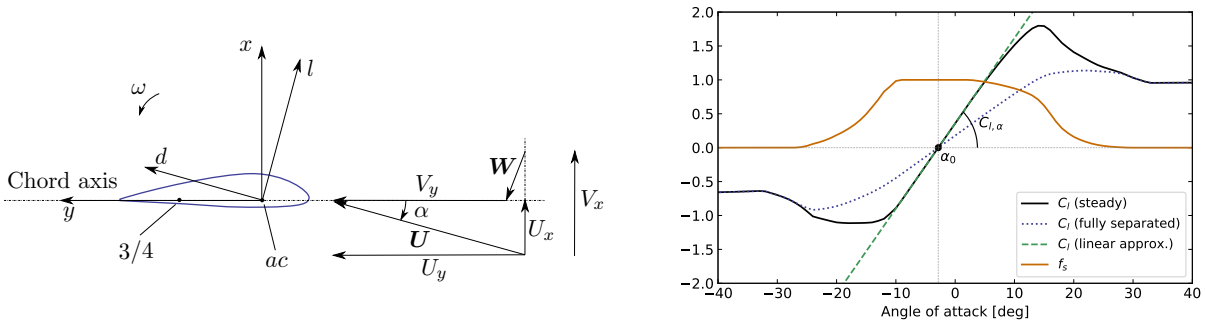


Figure 1: (Left) Notations for the aerodynamic models: relative velocity, $\boldsymbol{U}$, induced velocity, $\boldsymbol{W}$, undisturbed flow velocity, $\boldsymbol{V}$, aerodynamic center, 3/4 chord point, and pitching rate, $\omega$. (Right) Lift-coefficient functions for the FFA-W3-211 airfoils: steady, fully separated, and linear functions. The separation function, $f_s$, is also shown on the figure.

In order to write Equation 2 into a state-space form, we introduce an intermediate variable $\boldsymbol{W}_{\text{red}}$ defined as follows:

$$\boldsymbol{W}_{\text{int}} = \boldsymbol{W}_{\text{red}} + k\boldsymbol{W}_{\text{qs}} \tag{4}$$

Inserting Equation 4 into Equation 2 leads to:

$$\begin{aligned} \boldsymbol{W}_{\text{red}} + \tau_1 \dot{\boldsymbol{W}}_{\text{red}} &= (1-k)\boldsymbol{W}_{\text{qs}} \\ \boldsymbol{W} + \tau_2 \dot{\boldsymbol{W}} &= \boldsymbol{W}_{\text{red}} + k\boldsymbol{W}_{\text{qs}} \end{aligned} \tag{5}$$

The reduced induction eliminates the term $\dot{\boldsymbol{W}}_{\text{qs}}$, which greatly simplifies the formulation. The steady-state values of the different inductions, noted with a subscript 0, are:

$$\boldsymbol{W}_{0,\text{red}} = (1-k)\boldsymbol{W}_{0,\text{qs}}, \quad \boldsymbol{W}_{0,\text{int}} = \boldsymbol{W}_{0,\text{qs}}, \quad \boldsymbol{W}_0 = \boldsymbol{W}_{0,\text{qs}} \tag{6}$$

$\boldsymbol{W}_{\text{red}}$ is a continuous, scaled, and lagged version of the quasi-steady induction. $\boldsymbol{W}_{\text{int}}$ may be discontinuous if the quasi-steady induction is discontinuous. The smaller the value of $k$, the closer $\boldsymbol{W}_{\text{red}}$ is to $\boldsymbol{W}_{\text{qs}}$, the smaller the discontinuity of $\boldsymbol{W}_{\text{int}}$ would be if $\boldsymbol{W}_{\text{qs}}$ jumps between two values, and the slower the induced velocities will reach a steady state. The opposite occurs for larger values of $k$. The value $k = 0.6$ is widely used, but it should be noted that changing this value will affect the time response. The state-space formulation of the dynamic inflow model is directly obtained from Equation 5 as follows [1]:

$$\begin{bmatrix} \dot{\boldsymbol{W}}_{\text{red}} \\ \dot{\boldsymbol{W}} \end{bmatrix} = \begin{bmatrix} -\frac{1}{\tau_1}\boldsymbol{I}_2 & \boldsymbol{0} \\ \frac{1}{\tau_2}\boldsymbol{I}_2 & -\frac{1}{\tau_2}\boldsymbol{I}_2 \end{bmatrix} \begin{bmatrix} \boldsymbol{W}_{\text{red}} \\ \boldsymbol{W} \end{bmatrix} + \begin{bmatrix} \frac{1-k}{\tau_1} \\ \frac{k}{\tau_2} \end{bmatrix} \boldsymbol{W}_{\text{qs}} \tag{7}$$

where $\boldsymbol{I}_2$ is the $2 \times 2$ identity matrix.

### *2.2. Unsteady aerodynamics model*

The unsteady aerodynamic module of OpenFAST contains two variants of the Bedooes-Leishman dynamic stall model [16]. In this work, we added two additional models: the HGM model [7] and the Øye model. In this section, we present a version of the HGM model that is slightly modified compared to the original HGM model. We begin by presenting the parameters, inputs,

[1] Equation 7 is also found in [14, 15] but without the derivation steps presented above.

states, and outputs of the model. We then discuss the main differences with the HGM model and the HAWC2 implementation.

The model relies on a set of parameters that can be obtained from the lift, drag, and moment coefficients: $C_l$, $C_d$, and $C_m$, respectively. Of prime importance is the zero lift angle of attack, $\alpha_0$, and the lift slope at that location, $C_{l,\alpha}$. Based on these parameters, a separation function, $f_s$, and the fully separated lift coefficient, $C_{l,\text{fs}}$, may be calculated. Details on the calculation of $f_s$ and $C_{l,\text{fs}}$ may be found in [7]. We plot these functions in Figure 1 for the FFA-W3-211 airfoil, of 21.1% thickness, at a Reynolds number of 10M, as used in the International Energy Agency Wind Technology Collaboration Programme (IEA Wind) 15-MW reference wind turbine [17]. Additional parameters used by the model are the constants $A_1$, $A_2$, $b_1$, and $b_2$, which are used to model Wagner's memory function. In this work, we use the values from Jones: $A_1 = 0.165$, $A_2 = 0.335$, $b_1 = 0.0455$, $b_2 = 0.3$ [18].

The HGM model takes as input the angle of attack and the relative velocity norm at the 3/4 chord point ($\alpha_{34}$ and $U_{34}$, respectively) and the pitching rate of the airfoil section, $\omega$. The notations are illustrated on the left side of Figure 1. In the OpenFAST formulation, we use the velocity at the aerodynamic center $U_{ac}$ instead of $U_{34}$. Numerical investigations in [19] showed that changing the chord position where the velocity is computed has a negligible effect. The model uses four states ($x_1$–$x_4$) representing, respectively, two downwash memory terms representing the shed vorticity in the wake in attached flows, a lag to the attached lift, and the position of the separation point. The state equations are:

$$\dot{x}_1 = -T_u^{-1} b_1 \, x_1 + T_u^{-1} b_1 A_1 \alpha_{34} \tag{8}$$

$$\dot{x}_2 = -T_u^{-1} b_2 \, x_2 + T_u^{-1} b_2 A_2 \alpha_{34} \tag{9}$$

$$\dot{x}_3 = -T_p^{-1} x_3 + T_p^{-1} C_L^p \tag{10}$$

$$\dot{x}_4 = -T_f^{-1} x_4 + T_f^{-1} f_s(\alpha_F), \qquad x_4 \in [0, 1] \tag{11}$$

with the following definition of intermediate variables:

$$T_u(t) = \frac{1}{2} \min\left( \frac{c}{U_{ac}(t)}, 100 \right) \tag{12}$$

$$\alpha_E(t) = \alpha_{34}(t)(1 - A_1 - A_2) + x_1(t) + x_2(t) \tag{13}$$

$$C_L^p(t) = C_{l,\alpha} \, (\alpha_E(t) - \alpha_0) + \pi T_u(t) \omega(t) \tag{14}$$

$$\alpha_F(t) = \frac{x_3(t)}{C_{l,\alpha}} + \alpha_0 \tag{15}$$

where $T_f$ is the time constant characteristic of the trailing-edge stall, and $T_p$ is the time constant associated with the boundary layer pressure gradient. Both time constants are determined from $T_u$ as: $T_f = T_{f,0} T_u$ and $T_p = T_{p,0} T_u$, where $T_{f,0}$ and $T_{p,0}$ are user inputs, taken respectively as 6 and 1.5 in this study.

The outputs of the model are the dynamic airfoil coefficients $C_{l,\text{dyn}}$, $C_{d,\text{dyn}}$, and $C_{m,\text{dyn}}$. They are obtained from the states as follows:

$$C_{l,\text{dyn}}(t) = C_{l,\text{circ}} + \pi T_u \omega \tag{16}$$

$$C_{d,\text{dyn}}(t) = C_d(\alpha_E) + \left[ (\alpha_{34} - \alpha_E) + T_u \omega \right] C_{l,\text{circ}} + \left[ C_d(\alpha_E) - C_d(\alpha_0) \right] \Delta C''_{d,f} \tag{17}$$

$$C_{m,\text{dyn}}(t) = C_m(\alpha_E) - \frac{\pi}{2} T_u \omega \tag{18}$$

with the following intermediate variables:

$$C_{l,\text{circ}} = x_4 (\alpha_E - \alpha_0) C_{l,\alpha} + (1 - x_4) C_{l,\text{fs}}(\alpha_E) \tag{19}$$

$$\Delta C''_{d,f} = \frac{\sqrt{f^{st}(\alpha_E)} - \sqrt{x_4}}{2} - \frac{f^{st}(\alpha_E) - x_4}{4}, \qquad x_4 \geq 0 \tag{20}$$

Our current implementation differs from the HGM model on several points: 1) the acceleration term $\dot{U}_{\text{ac}}$ is neglected, 2) the influence of the dynamic lift on the moment is neglected, and 3) the dynamic drag coefficient uses $C_{l,\text{circ}}$ instead of $C_{l,\text{dyn}}$ and therefore includes a different torsional component ($T_u \omega C_{l,\text{circ}}$). These assumptions are also included in the HAWC2 formulation and discussed in [20]. The reader is referred to the original work of Hansen et al. [7] for more details on the different terms present in the state and output equations. In particular, the analytical linearization of the state equations is present in this reference. We note that Øye's dynamic stall model consists of using Equation 11 but taking the actual angle of attack instead of $\alpha_F$. The model was therefore readily added to OpenFAST. The OpenFAST implementation uses the continuous formulation presented above. A discrete form of the state equation may be obtained by integrating the state equations between two time steps. For instance, the discrete form of Equation 8 and Equation 9 would be implemented as:

$$x_i^n = x_i^{n-1} e^{-\Delta t b_i / T_u} + \frac{1}{2}(\alpha_{34}^n + \alpha_{34}^{n-1}) A_i \left[1 - e^{-\Delta t b_i / T_u}\right], \quad i \in \{1, 2\} \tag{21}$$

where the superscript $n$ indicates the time step index, and $\Delta t$ is the time step.

HAWC2 uses a similar variation of the HGM model, as detailed in [20]. The main differences with our implementation are the following: a different definition of the effective angle of attack is used, the states $x_1$ and $x_2$ are scaled by the velocity, and their update is scaled by $f_s$ (taken as $x_4^{n-1}$). In HAWC2's formulation, these variables are obtained as follows [20]:

$$x_i^n = x_1^{n-1} e^{-\Delta t b_i / T_u} + (\alpha_{34}^n U_{34}^n - \alpha_{34}^{n-1} U_{34}^{n-1}) \frac{A_i}{b_i} \frac{T_u}{\Delta t} \left[1 - e^{-\Delta t b_i / T_u}\right] x_4^{n-1}, \quad i \in \{1, 2\} \tag{22}$$

$$\alpha_E^n = \alpha_{34}^n - \frac{x_1^n}{U_{34}^n} - \frac{x_2^n}{U_{34}^n} \tag{23}$$

which may be compared to Equation 21 and Equation 13. In attached flow, when $x_4 = 1$, this modification produces the same results as the original formulation. When the flow starts to separate, the attached flow part of the model is phased out as a function of the separation point position, leading to $\alpha_E = \alpha_{34}$ when operating in full separation. These differences will be kept in mind when comparing results from both OpenFAST and HAWC2. HAWCStab2 currently uses a continuous formulation similar to ours but will be updated in the future to match the formulation of HAWC2.

## 3. Results

In this section, we present different verifications and applications of the two models introduced in section 2.

### *3.1. Time series verification of the dynamic stall model*

We verify the implementation of the dynamic stall model presented in subsection 2.2 by performing simulations with sinusoidal pitching of an airfoil section about its mid-chord point. The airfoil selected is the FFA-W3-211 airfoil, for which the lift coefficient was presented in Figure 1. The airfoil chord is set to $c = 1$ m and the free-stream to $U_0 = 10$ m.s$^{-1}$. The airfoil is pitched at two frequencies, $f = 1$ and $f = 2$ Hz, with an amplitude of 10 deg, around the mean angles $-5$ deg and 20 deg. The reduced frequencies are $k_\omega = \pi f c / U_0 = 0.31$ and $k_\omega = 0.63$. The dynamic airfoil coefficients obtained with OpenFAST and HAWC2 are shown in Figure 2 for these two frequencies. A satisfying agreement is found between the two tools, therefore verifying the OpenFAST implementation. As noted in subsection 2.2, the differences in the formulation of $x_1$, $x_2$, and $\alpha_E$ between the two tools is the main source of differences found in the different coefficients. This was confirmed using a Python implementation of the method.

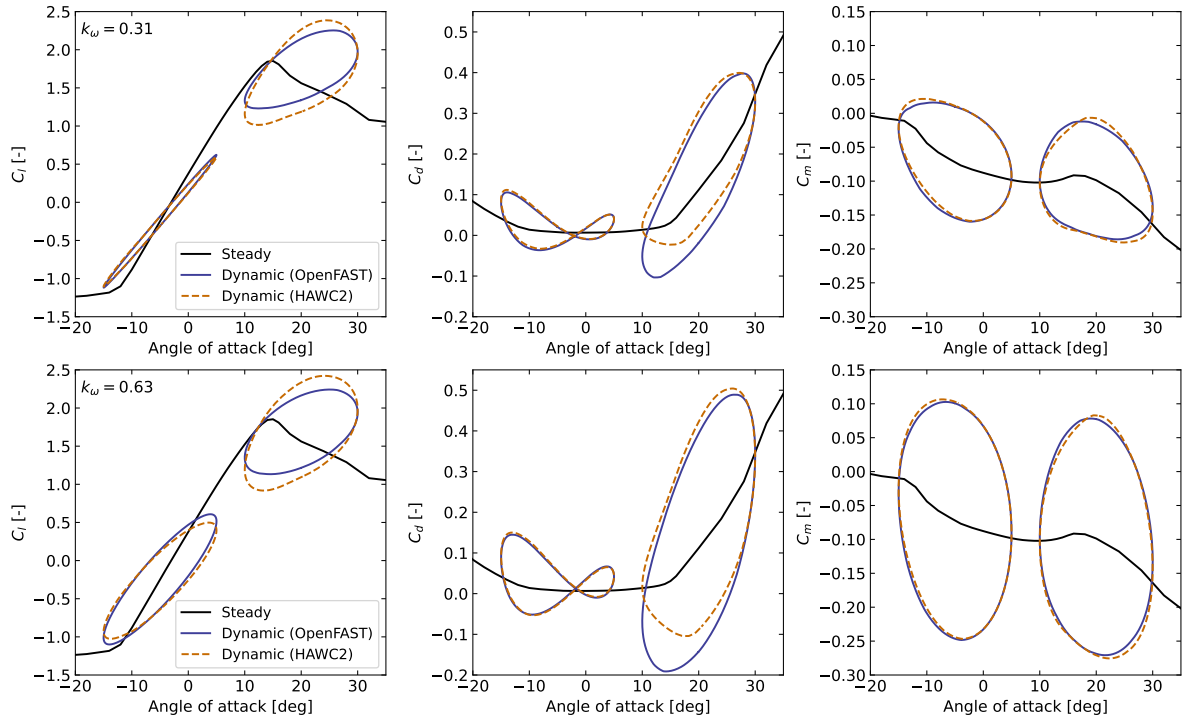


Figure 2: Dynamic airfoil coefficients obtained from a sinusoidal pitching of an airfoil section about its mid chord. Top plots are for $k_\omega = 0.31$; bottom plots are for $k_\omega = 0.63$.

These differences are expected to be more pronounced for larger angles of attack because HAWC2 uses a scaling proportional to $f_s$. The dynamic stall loops become more "open" as the reduced frequency increases, leading to increased lag between the angle of attack and the forces. Such lag will have a consequence on the aerodynamic stiffness and damping, as we will discuss in subsection 3.3.

### *3.2. Dynamic inflow model*

To illustrate the implementation of the new dynamic inflow model of OpenFAST, a pitch-step simulation is performed. Pitch-step events abruptly change the circulation along the blade and are therefore a common test case for dynamic inflow models (see, e.g., [21, 22]). We use the NREL 5-MW wind turbine [23], with all degrees of freedom off, a constant rotational speed of $\Omega = 9.161$ rpm and a uniform wind speed of $U_0 = 8$ m.s$^{-1}$. The pitch step of 4 deg is illustrated in Figure 3 together with the aerodynamic torque and axial induction responses obtained for different values of $\tau_1$. The value of $\tau_1 = 15.9$ s corresponds to the application of Equation 1 for the conditions prior to the pitch step. The response is consistent with the expected behavior of the dynamic inflow models: a change of circulation at the rotor takes time to propagate downstream until the wake reaches a new steady state. In this model, this is implemented by a delay between two quasi-steady induction values (Equation 7).

Dynamic inflow effects are important to properly capture the aerodynamic response of the rotor to changes in inflow or operating conditions. In particular, this effect may be important for the stability of the turbine in a closed-loop situation. To illustrate this, we numerically computed the transfer function from the collective pitch angle of the controller to the rotor speed. A rigid model of the NREL 5-MW turbine is used with varying rotor speed, wherein the generator torque is set to follow the optimal tip-speed ratio. Simulations with sinusoidal variations of the pitch at various frequencies are performed; the amplitude and phase of the rotor speed are

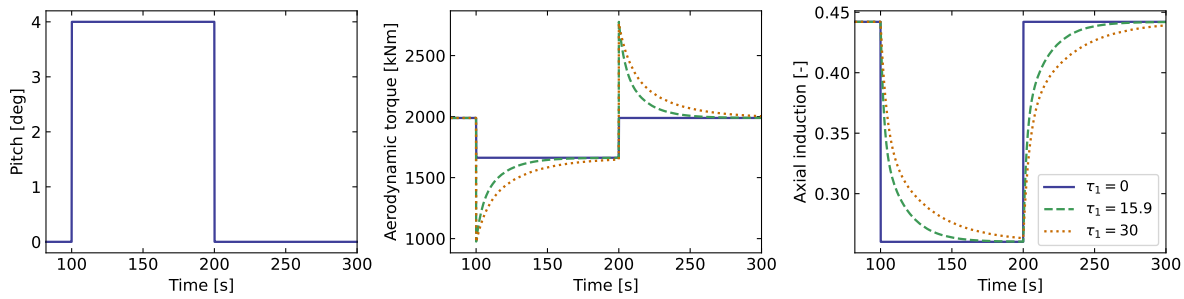


Figure 3: Aerodynamic torque and axial induction responses to a pitch step using the newly implemented dynamic inflow model for different values of the time constant $\tau_1$. The rotor operates at a constant rotational speed.

then extracted and used to compute the transfer function. Results for different time constants, $\tau_1$, are shown in Figure 4. The rotor speed frequency is indicated with a dashed vertical line on the figure, corresponding to a rotor speed of 9.14 rpm. As observed from the figure, the

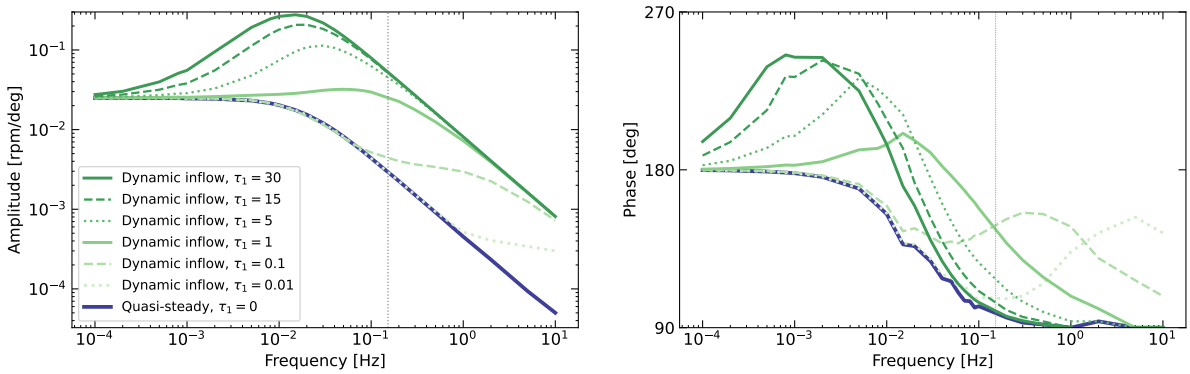


Figure 4: Effect of dynamic inflow on the transfer function from collective pitch angle to rotor speed for a closed-loop drivetrain where the generator follows the optimal tip-speed ratio.

dynamic inflow amplifies the rotor speed response compared to a case with no dynamic inflow (quasi-steady wake). In general, the pitch and rotor speed signals are found to be 90 deg out of phase at frequencies large enough compared to the frequency associated with the time scale ($f \gg 1/\tau_1$ where $f$ is the frequency) and 180 deg out of phase at low frequencies ($f \ll 1/\tau_1$). The time constants associated with the dynamic inflow model are typically large. For the NREL 5-MW turbine, $\tau_1 \approx 15$ s. For this realistic value, the impact of the dynamic inflow model is primarily observed for frequencies an order of magnitude smaller than the rotor speed frequency. At low frequencies ($f \ll 1/\tau_1$), the dynamic inflow model stops having an effect because the generator speed adjusts continuously to the slow changes in aerodynamic torque induced by the pitch variation, and the dynamic inflow model has enough time to react: the inductions are always in equilibrium, similar to a quasi-steady inflow. At high frequencies, the dynamic inflow behaves like a frozen wake where the induced velocities remain constant, which differs from the quasi-steady approach.

### *3.3. Linearization and stability analyses*

The main motivation for using the two aerodynamic models presented in section 2 is the possibility to include their effects when performing linearization with OpenFAST. OpenFAST only supports linearization for continuous-time models, such as the ones newly implemented.

Linearization is useful to perform stability analyses of wind turbines, often represented using a Campbell diagram showing the frequency and damping of the different turbine modes as functions of the operating conditions.

We generated Campbell diagrams for the NREL 5-MW wind turbine using different model options for the dynamic stall and dynamic inflow model, and using both OpenFAST and HAWCStab2. For each wind speed, a fixed rotor speed and pitch is used, meaning that the dynamics of the controller are not accounted for and the drivetrain torsion is therefore a "fixed-free" mode. The system is linearized about the periodic equilibrium point, accounting for the deflection of the wind turbines. The influence of the dynamic stall model on the Campbell diagram of the turbine is shown in Figure 5 using results from OpenFAST and HAWCStab2. The impact of the dynamic stall is primarily observed in the flapwise modes

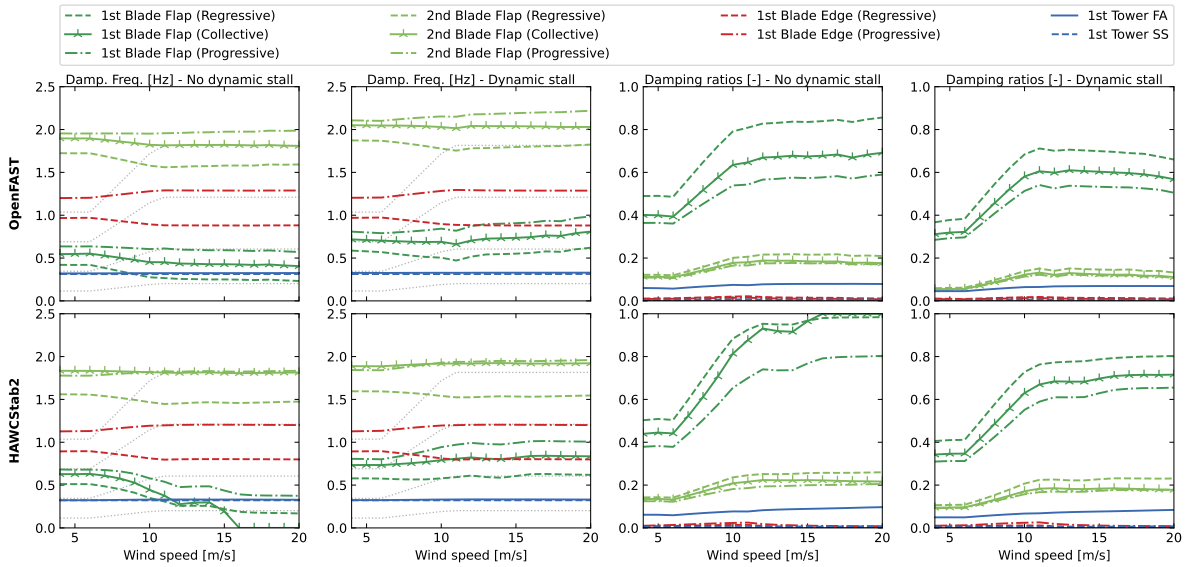


Figure 5: Campbell diagram of the NREL 5-MW wind turbine with or without the dynamic stall contribution as obtained by OpenFAST (top) and HAWCStab2 (bottom). From left to right: damped frequencies without dynamic stall, damped frequencies with dynamic stall, damping ratio without dynamic stall, damping ratio with dynamic stall. The dotted lines indicate the $1p$, $3p$, $6p$ and $9p$ frequencies, where $p$ is the rotational speed frequency.

of the turbine. Small effects on the frequencies and damping of the tower and edgewise modes can be observed. Capturing the correct edgewise damping is important because these modes have typically significantly lower damping than the flapwise modes. But in this study, the impact of the dynamic stall on the damping of the edgewise modes was found to be limited. Different conclusions may be obtained for different blade designs. The HAWCStab2 frequencies of the first flapwise mode are observed to be overdamped when dynamic stall is not active; however, the results from OpenFAST and HAWCStab2 are consistent. We observe that the damped frequencies of the flapwise modes increase compared to the case without dynamic stall. The same is found for the natural frequencies (not shown), and they show an increased dependency on the wind speed when dynamic stall is turned on. The damping of the flapwise modes are reduced when the dynamic stall model is included, contributing to the increase of the damped frequency as well. The dynamic stall model is therefore observed to contribute to aerodynamic stiffening and a reduced aerodynamic damping of the flapwise modes. Such contributions can be explained from the lag introduced by the attached flow part of model, which introduces a phase shift between the motion of the blade and the aerodynamic force and reduces the force amplitude.

The results presented in Figure 5 were generated without dynamic inflow, using a "frozen wake" approach. Both OpenFAST and HAWCStab2 can perform linearization analyses with different wake models: quasi-steady wake, frozen wake, or dynamic wake. In the quasi-steady wake approach, the induced velocities at the rotor are instantaneously set to the equilibrium value, which corresponds to $\tau_1 = 0$. In the frozen wake approach, the induced velocities at the rotor do not change, corresponding to $\tau_1 = \infty$. The wake state is relevant when performing linearization because linearization reflects how the system states change when the system is perturbed. As illustrated in Figure 3, smaller changes in aerodynamic forces and larger changes in the inductions are expected in the quasi-steady approach ($\tau_1 = 0$), whereas the frozen wake and dynamic wake approaches are expected to show larger force variations about the operating point because of the slow adaptation of the induction to the perturbations (infinitely slow for the frozen wake).

In Figure 6, we investigate the effect of the wake and dynamic inflow models on the first collective flapwise mode of the turbine using OpenFAST and HAWCStab2, this time plotting the natural frequencies.

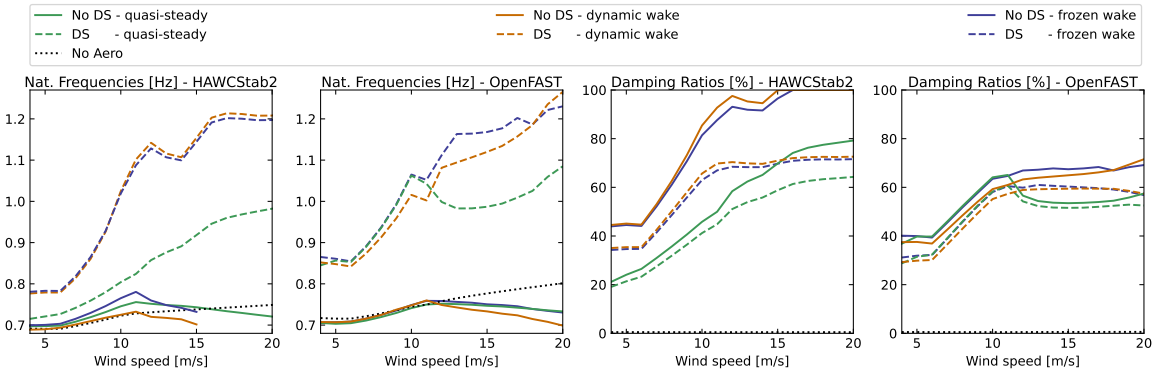


Figure 6: Influence of dynamic stall and wake models on the first collective flapwise mode natural frequencies and damping as obtained with OpenFAST and HAWCStab2. "DS" = dynamic stall; "No DS" = no dynamic stall.

The influence of the dynamic stall model has a clear impact on the natural frequencies and damping. The main trends discussed earlier are captured by OpenFAST and HAWCStab2 (for instance, comparing "No DS - frozen wake" with "DS - frozen wake"): 1) the frequencies are increased when the dynamic stall model is used, and aerodynamic stiffening happens with increased wind speed; 2) the dynamic stall model decreases the damping. Both tools agree on the trends, but the difference in magnitudes indicates some underlying differences in the tools or model parameters.

The influence of the wake model is not as clear. The damping in HAWCStab2 is significantly higher when quasi-steady or dynamic wake are used without the dynamic stall model, leading to overdamped frequencies. When the dynamic stall model is turned off, the OpenFAST results show limited differences between the quasi-steady, dynamic, and frozen wake results in terms of frequencies, but differences are visible in the damping ratios. Intuitively, and in light of the values of $\tau_1$ discussed earlier, one could expect the dynamic wake results to be between the frozen wake and quasi-steady wake (the orange lines would be in between the green and blue lines on the figure). In practice, we only observe this for some of the cases. It appears that the two tools behave differently in their handling of the wake dynamics, which can also be a result of how the blade element momentum algorithm is implemented by each tool. Overall, the dynamic wake model increases the damping compared to a quasi-steady wake, but the impact of using the dynamic wake over the frozen wake is limited.

We conclude this study by inspecting the changes in frequencies and damping ratios of the first eight modes of the wind turbine. We compare the modal parameters obtained with: 1) no aerodynamic forces; 2) no dynamic stall and a frozen wake, which corresponds to the baseline model of OpenFAST before this work; 3) dynamic stall and dynamic wake. The structural frequencies at 4 m.s$^{-1}$ are used as a reference to evaluate the relative change in frequencies. The damping ratios are compared in absolute terms. The results are shown in Figure 7. HAWCStab2

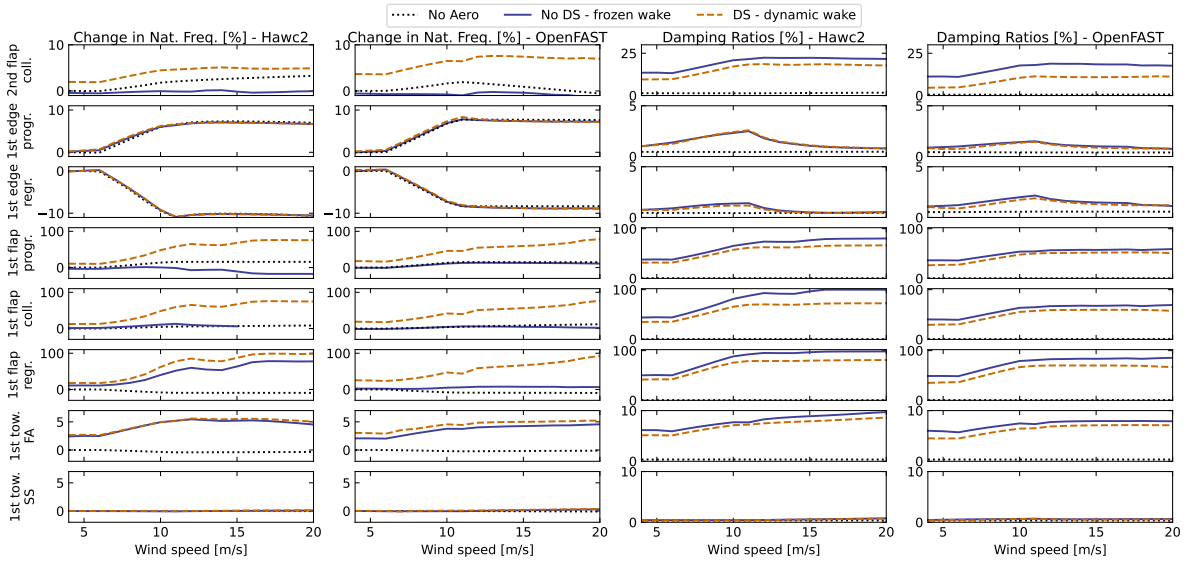


Figure 7: Relative change in natural frequencies (two left plots) compared to the structural frequency ("No Aero") at 4 m.s$^{-1}$ and absolute change in damping ratios (two right plots) due to aerodynamic loads as obtained from HAWCStab2 and OpenFAST.

predicts higher aerodynamic damping for the flapwise modes than OpenFAST. The quasi-steady wake implementations of HAWCStab2 and OpenFAST predict different changes in frequencies for the flap modes (in particular the regressive and progressive modes), but these differences are reduced when both the dynamic wake and dynamic stall models are used. The differences are likely attributed to differences in the BEM implementations. Overall, results from OpenFAST and HAWCStab2 are in fair agreement and reveal similar trends. The main conclusions drawn from Figure 7 are as follows:

- The tower side-side mode is not influenced by the aerodynamic loads.
- Both the damping and frequency of the tower fore-aft mode are influenced by the aerodynamic loads. The presence of aerodynamic loads increases the natural frequency by 2% below the rated wind speed and by 5% above the rated wind speed. The damping ratio increases from 6% below the rated wind speed to 8% above the rated wind speed. The dynamic stall model reduces the tower fore-aft damping ratio by about 1%.
- The centrifugal stiffening increases the blade collective frequency by 5% for this turbine (visible in the "No aero" curve).
- The dynamic stall model significantly stiffens the blade flapwise modes. The frequency of the first flapwise modes are increased by about 10% below the rated wind speed, and nearly 100% at high wind speeds. The relative change in frequency is more significant for the regressive mode because the frequency obtained without aerodynamic load also decreases with the rotational speed. Without the dynamic stall model, the first flapwise frequencies remain close to the values without aerodynamic loads.

- The aerodynamic damping ratio of the first flapwise modes reaches values between 50% below the rated wind speed to 100% above the rated wind speed. The dynamic stall model removes 10%–20% from the damping ratio value of the flapwise modes.
- The frequencies of the regressive and progressive edgewise modes are not observed to be strongly affected by the aerodynamic loads, but the loads are seen to add 1%–2% to the damping ratio.
- The aerodynamic effects on the second flapwise modes are similar to the ones observed for the first flapwise modes, but less significant: about 5% increase in frequency and 10%–20% of additional damping.

The trends listed above are expected, but they may vary in proportion for different wind turbine designs.

## 4. Conclusions and future work

In this work, a new dynamic inflow model and two unsteady aerodynamics models were added to OpenFAST. The models were expressed in state-space form and using a continuous-time formulation, which facilitates their linearization. The features were verified against HAWC2 and HAWCStab2 in the time domain and frequency domain, respectively. These new features allow for the calculation of the system frequencies of wind turbines that accounts for the stiffening, damping, and inertial contributions from the aerodynamics. Such contributions are important to study the aeroelastic stability of wind turbines. Thanks to the development presented in this work, Campbell diagrams accounting for dynamic stall and dynamic wake effects were generated for the first time with OpenFAST. It was observed that the dynamic stall model increases the flapwise frequencies of the turbine while reducing the damping of these modes. For the NREL 5-MW wind turbine, the natural frequencies of the first flapwise modes of the blade are increased by up to 100%, and the frequency of the first tower fore-aft mode is increased by up to 5% compared to values without aerodynamic loads. The aerodynamic loads contribute to damping ratios of about 75% for the first flapwise modes and 7% for the first tower fore-aft mode. A limited effect on the side-side and edgewise modal parameters was observed. The dynamic inflow model was observed to have limited influence on the system frequencies and damping compared to a frozen-wake approach. Both OpenFAST and HAWCStab2 showed consistent results regarding the change of frequencies and damping associated with the dynamic stall model.

Extensions of OpenFAST for hydrokinetic turbines are currently being developed, and we expect that the dynamic stall and wake effects will be essential for a complete description of the system stability. The topic of aeroelastic stability of wind turbines is therefore an important priority for future work.

## Acknowledgments

The support of various experts at NREL, Technical University of Denmark, and Envision has been critical to the completion of this work. Their contribution is gratefully acknowledged. This work was authored in part by the National Renewable Energy Laboratory, operated by Alliance for Sustainable Energy, LLC, for the U.S. Department of Energy (DOE) under Contract No. DE-AC36-08GO28308. Funding provided by Envision Energy USA Ltd under the Funds in Agreement contract number 17-1834.

## References

[1] D. M. Volk, B. S. Kallesøe, S. Johnson, G. R. Pirrung, R. Riva, and F. Barnaud. Large wind turbine edge instability field validation. *Journal of Physics: Conference Series*, 1618:052014, sep 2020.
[2] M. H. Hansen. Aeroelastic stability analysis of wind turbines using an eigenvalue approach. *Wind Energy*, 7(2):133–143, 2004.
[3] J. M. Jonkman and B. J. Jonkman. FAST modularization framework for wind turbine simulation: full-system linearization. *Journal of Physics: Conference Series*, 753:082010, sep 2016.
[4] R. P. Coleman and A. M. Feingold. Theory of self-excited mechanical oscillations of helicopter rotors with hinged blades. Technical report, NACA TN 1351, 1958.
[5] J. M. Jonkman, E. Branlard, and J. P. Jasa. Influence of wind turbine design parameters on linearized physics-based models in openfast. *Wind Energy Science*, 7(2):559–571, 2022.
[6] H. Snel and J. G. Schepers. Joint investigation of dynamic inflow effects and implementation of an engineering method. Technical report, ECN-C–94-107, Energy Research Centre of the Netherlands, Petten, 1995.
[7] M. H. Hansen, M. Gaunaa, and H. A. Madsen. A Beddoes-Leishman type dynamic stall model in state-space and indicial formulations. Technical report, Risø National Laboratory, Roskilde, Denmark, 2004.
[8] T. S. Beddoes. A near wake dynamic model. *proc. of the AHS national specialist meeting on aerodynamics and aeroacoustics*, 1987.
[9] S. Øye. Dynamic stall, simulated as a time lag of separation. *Proceedings of the 4th IEA Symposium on the Aerodynamics of Wind Turbines*, 1991.
[10] T. J. Larsen and A. M. Hansen. *HAWC2 - User manual*. DTU-Risø-R-1597, 2007.
[11] H. A. Madsen, T. J. Larsen, G. R. Pirrung, A. Li, and F. Zahle. Implementation of the blade element momentum model on a polar grid and its aeroelastic load impact. *Wind Energy Science*, 5(1):1–27, 2020.
[12] M. H. Hansen. Aeroelastic properties of backward swept blades. *49th AIAA Aerospace Sciences Meeting including the New Horizons Forum and Aerospace Exposition*, 2011.
[13] E. Branlard. *Wind Turbine Aerodynamics and Vorticity-Based Methods: Fundamentals and Recent Applications*. Springer International Publishing, 2017.
[14] N. S. Mangat. *Reduced order wind turbine aeroelastic modelling for condition monitoring & fault detection*. PhD thesis, Delft University of Technology, 2019.
[15] J. Geisler. Simplified dynamic inflow for control engineering models. *Journal of Physics: Conference Series*, 2022.
[16] R. Damiani and G. Hayman. The unsteady aerodynamics module for fast 8. Technical report, National Renewable Energy Laboratory, 2017.
[17] E. Gaertner, J. Rinker, L. Sethuraman, F. Zahle, B. Anderson, G. Barter, N. Abbas, F. Meng, P. Bortolotti, W. Skrzypinski, G. Scott, . Feil, H. Bredmose, Katherine Dykes, M. Shields, C. Allen, and A. Viselli. Definition of the IEA 15-megawatt offshore reference wind turbine. Technical report, International Energy Agency, 2020.
[18] R. T. Jones. Operational treatment of the non-uniform lift theory in airplane dynamics. Technical report, NASA, Technical Note 667, 1938.
[19] A. Li, M. Gaunaa, G. R. Pirrung, A. Meyer Forsting, and S. G. Horcas. How should the lift and drag forces be calculated from 2-d airfoil data for dihedral or coned wind turbine blades? *Wind Energy Science Discussions*, 2022:1–40, 2022.
[20] G. R. Pirrung and M. Gaunaa. Dynamic stall model modifications to improve the modeling of vertical axis wind turbines. Technical report, Technical University of Denmark - Wind Energy - E-0171, 2018.
[21] E. Branlard and M. Gaunaa. Superposition of vortex cylinders for steady and unsteady simulation of rotors of finite tip-speed ratio. *Wind Energy*, 19(7):1307–1323, 2015.
[22] M. O. L. Hansen. *Aerodynamics of Wind Turbines - Second Edition*. Earthscan, London, Sterling, VA, 2008.
[23] J. Jonkman, S. Butterfield, W. Musial, and G. Scott. Definition of a 5mw reference wind turbine for offshore system development. Technical Report NREL/TP-500-38060, National Renewable Energy Laboratory, 2009.